

# Structural, Optical, Magnetic and Photocatalytic Properties of $\text{Sr}_2\text{Nb}_2\text{O}_7\text{-Nb}_2\text{O}_5\text{-SrCO}_3$ Nanocomposite Synthesized by Solvothermal Route

Ziba davtalab nazarlou

Urmia University

Leila Kafi-Ahmadi (✉ [l.kafiahmadi@urmia.ac.ir](mailto:l.kafiahmadi@urmia.ac.ir))

Urmia University <https://orcid.org/0000-0001-8947-2706>

shahin khademinia

Semnan University Faculty of Chemistry

---

## Research Article

**Keywords:** Inorganic, photocatalytic, morphologies, ferroelectric

**Posted Date:** June 30th, 2020

**DOI:** <https://doi.org/10.21203/rs.3.rs-38132/v1>

**License:**  This work is licensed under a Creative Commons Attribution 4.0 International License. [Read Full License](#)

---

# Abstract

Sr<sub>2</sub>Nb<sub>2</sub>O<sub>7</sub> nanocomposites were prepared by a low cost ultrasonic assisted solvothermal method between Sr(NO<sub>3</sub>)<sub>2</sub> and Nb<sub>2</sub>O<sub>5</sub> at stoichiometric Sr:Nb molar ratio. The synthesized nanomaterials were characterized by X-ray powder diffraction (XRPD) technique. Rietveld analysis showed that the obtained materials were crystallized well in the orthorhombic crystal structure with the space group Cmc2<sub>1</sub>. The morphologies of the synthesized materials were studied by field emission scanning electron microscope (FESEM). Strong light absorption in the ultraviolet light region at about 320 nm was observed for the synthesized nanocomposites by Ultraviolet-visible spectra. Vibrating-sample magnetometer (VSM) analysis showed that the as-synthesized nanomaterials had ferromagnetic property. Photocatalytic performance of the synthesized nanocomposites was investigated for the degradation of Malachite Green (MG) water pollutant in aqueous solution under visible light condition. The light source was a white color fluorescent lamp with the light power of 40 W and the light intensity of 920 lm/m<sup>2</sup> (1.34 W/m<sup>2</sup>). Design expert software was used to find the optimum conditions. The optimum conditions were found as 0.61 mL H<sub>2</sub>O<sub>2</sub>, 40 mg catalyst, and 60 min. The as prepared MG solution volume and concentration were 80 mL and 50 ppm, respectively, to achieve the optimum conditions. The kinetic study showed that the photodegradation process followed a first order reaction model.

## 1. Introduction

Strontium pyroniobate with a perovskite layer structure is a ferroelectric material. The compound is interesting due to its several applications as a nonvolatile ferroelectric memory [1], optical waveguides [2] and a variety of other applications [3,4]. Besides, the compound has been studied extensively for the photocatalytic water splitting reaction under ultraviolet irradiation [5–9]. So, Strontium pyroniobate, Sr<sub>2</sub>Nb<sub>2</sub>O<sub>7</sub>, has attracted considerable attention due to its high potential as a novel photocatalyst for hydrogen production from water [10–12]. Also, there is another possible application found for Sr<sub>2</sub>Nb<sub>2</sub>O<sub>7</sub>. It has been found that Sr<sub>2</sub>Nb<sub>2</sub>O<sub>7</sub> is a candidate material for high-temperature piezoelectric sensor in automobiles, thermal power plants, and nuclear power plants [13]. There are several methods have been reported for the synthesis of Sr<sub>2</sub>Nb<sub>2</sub>O<sub>7</sub>, including solvothermal method at 240 °C for 48 h [12], sol–gel [14], PC molten salt route [13], sol–gel electrophoresis [15], solid state [16] and solvothermal method at 200 C for 24 h [17]. At room temperature, Sr<sub>2</sub>Nb<sub>2</sub>O<sub>7</sub> possesses orthorhombic unit cell parameters with a = 3.933, b = 26.726, and c = 5.683 Å [3]. The crystal structure of Sr<sub>2</sub>Nb<sub>2</sub>O<sub>7</sub> have vertex sharing NbO<sub>6</sub> octahedral units that are separated by additional O atoms [18–21]. Sr<sub>2</sub>Nb<sub>2</sub>O<sub>7</sub> is included in a class having a chemical composition of Sr<sub>n</sub>Nb<sub>n</sub>O<sub>3n+2</sub> [22] where n is the number of NbO<sub>6</sub> octahedrons. Only n = 4 and n = 5 members of the series have been observed [22–24]. When Sr<sub>2</sub>Nb<sub>2</sub>O<sub>7</sub> is cooled from above the Curie temperature, it undergoes the ferroelectric phase transition from space group Cmc<sub>2</sub> to Cmc2<sub>1</sub>, which is referred to the normal orthorhombic phase [25]. By cooling the crystal phase to 215 °C, the compound undergoes a crystal phase change to an incommensurate phase with the space group Cmc2<sub>1</sub> [26,27].

MG is used in several industrial and commercial processes such as leather, paper, silk, cotton, and jute dyeing processes. Besides, MG is used in fisheries and aquaculture industry as an antifungal and anti-protozoan agent. Because MG is a non-biodegradable dye, it has now become a compound with highly risk due to its effects on the immune system. Also, MG causes mutagenic, carcinogenic, and teratogenic effects to living organisms [28]. Furthermore, several researches have been done on the risks of using MG on the human health. It has been found that MG should not be used for beverages, food and medicines because it can cause skin irritation, blurred vision, etc [29]. So, finding methods to remove this dye pollutant efficiently from the industrial waste water is needed. In recent years, heterogeneous photocatalysis has received much attention since it can be used to deal with wastewater pollutants [30]. Because of the above mentioned reasons, the present work focuses to study the performance of the as-synthesized semiconductor nanocomposites for the degradation of MG.

In the present study, a simple solvothermal route was studied for the synthesis of Sr<sub>2</sub>Nb<sub>2</sub>O<sub>7</sub> nanocomposites using Nb<sub>2</sub>O<sub>5</sub>, Sr(NO<sub>3</sub>)<sub>2</sub> and NaOH raw materials. As per our knowledge, there is no information in the literature about the synthesis of the nanostructures under the present conditions. VSM analysis of the as-prepared nanocomposites is also reported in the present work for the first time. The photodegradation of MG in aqueous solutions under visible light condition is studied by the synthesized Sr<sub>2</sub>Nb<sub>2</sub>O<sub>7</sub> nano-photocatalyst. Design expert 7 software was used to optimize the values of the factors including H<sub>2</sub>O<sub>2</sub> volume, photocatalyst amount and photocatalytic degradation time affect on the photodegradation process. Excellent photocatalytic efficiency was achieved under the applied optimized conditions.

## 2. Experimental

### 2.1. Materials and instruments

The raw materials including Nb<sub>2</sub>O<sub>5</sub>, Sr(NO<sub>3</sub>)<sub>2</sub> and KOH were of analytical grade, used without further purifications and purchased from Merck Company. A X-ray powder diffractometer D5000 (Siemens AG, Munich, Germany) using CuK<sub>α</sub> radiation was used to study the crystal phase properties of the as-synthesized nanocomposites. The rietveld analysis done by FullProf software was used to make the quantification and crystal phase type study of the synthesized materials. A field emission scanning electron microscope (Hitachi FE-SEM model S-4160) was used to study the morphology of the obtained materials. The as-prepared nanomaterials were dispersed in water and cast onto a copper grid to study the sizes and morphology of the synthesized materials by TEM (Transmission Electron Microscope) using a Philips – CM300 - 150 KV microscope. Absorption spectra were recorded on a UV-visible spectrophotometer model-UV-1650 PC (Shimadzu, Japan). Also, magnetic measurements were carried out with a vibrating sampling magnetometer (VSM, Model 7400-LakeShore). The photocatalytic performance of the synthesized Sr<sub>2</sub>Nb<sub>2</sub>O<sub>7</sub> nanocatalysts for the degradation of MG was investigated in the presence of H<sub>2</sub>O<sub>2</sub> (30%, w/w) under visible light irradiation at room temperature. A digital Lux meter model GM 1010 was used to measure the light intensity of the irradiated light used in the photocatalytic process.

## 2.2. Solvothermal synthesis of Sr<sub>2</sub>Nb<sub>2</sub>O<sub>7</sub> nanocomposites

In a typical experiment for the synthesis of S<sub>1</sub>, 1.05 g (5 mmol) of Sr(NO<sub>3</sub>)<sub>2</sub>·5H<sub>2</sub>O (Mw = 211.62 g mol<sup>-1</sup>) was added into a 10 mL of ethyl alcohol at room temperature and stirred for 15 min. Then, 0.66 g (2.5 mmol) of Nb<sub>2</sub>O<sub>5</sub> (Mw = 265.82 g mol<sup>-1</sup>) was added to 20 mL of a 1:1 V/V deionized distilled water and ethyl alcohol and stirred for 15 min. The solution was added to the previous obtained mixture and stirred more for 15 min. The pH value of the resultant solution was adjusted at 12 by a 1 molar NaOH solution. The resultant solution was stirred for further 15 min and then ultrasonicated for 30 min. The final solution was transferred into a 100-mL Teflon lined stainless steel autoclave. The autoclave was sealed and heated in an electrical oven at 120 °C (S<sub>1</sub>) and 180 °C (S<sub>2</sub>) for 48 h, 180 °C (S<sub>3</sub>) and 200 °C (S<sub>4</sub>) for 96 h. When the reaction was completed, the autoclave was cooled to room temperature normally in the oven. The prepared white color powder was filtered, washed with distilled water and dried at 120 °C for 20 min under normal atmospheric conditions. The final obtained powder was treated thermally in a furnace at 400 °C for 3 h.

## 3. Results And Discussions

### 3.1. Characterization

The as-synthesized Sr<sub>2</sub>Nb<sub>2</sub>O<sub>7</sub> composites are studied by X-ray powder diffraction analysis (Figure 1). Structural analysis was done by the *FullProf* program, employing profile matching with constant scale factor. The calculated crystal phase type results of the profile matching analysis (full lines) is shown in the figure. The results show that changing the reaction condition decreases the main phase percent in the composite mixture. The XRPD pattern for S<sub>1</sub> has a main Sr<sub>2</sub>Nb<sub>2</sub>O<sub>7</sub> crystal structure (blue bars) with the space group Cmc2<sub>1</sub>. Lattice parameters were found as a=3.9 Å, b=26.6 Å, c=26.6 Å. The data revealed that the other crystal phases in the composite were Nb<sub>2</sub>O<sub>5</sub> (red bars) and SrCO<sub>3</sub> (green bars).

Cell parameters, grain size, dislocation density, strain, quantitative phase analysis and rietveld analysis refinement data for S<sub>1</sub> to S<sub>4</sub> are presented in Table 1. Direct comparison method was used to study the quantitative phase analysis. According to the method, the experimental line intensity of the impurity phases (Nb<sub>2</sub>O<sub>5</sub> and SrCO<sub>3</sub>) present in the mixture are compared to a line from the main phase (Sr<sub>2</sub>Nb<sub>2</sub>O<sub>7</sub>) in the mixture. In a typical process, the peaks with highest intensity for each phase at 25.18°, 32.46° and (54.57° (S<sub>1</sub> and S<sub>2</sub>) 47.66° (S<sub>3</sub>) and 24.10° (S<sub>4</sub>)) for Nb<sub>2</sub>O<sub>5</sub>, SrCO<sub>3</sub> and Sr<sub>2</sub>Nb<sub>2</sub>O<sub>7</sub>, respectively, are chosen. Also, the crystallite size data D (nm) of the obtained nanomaterials were calculated by Scherrer equation (Table 1):

$$D = \frac{K\lambda}{B_{1/2} \cos\theta}$$

In this equation, D is the entire thickness of the crystalline sample, λ is the X-ray diffraction wavelength (0.154 nm), K is the Scherrer constant (0.9), B<sub>1/2</sub> of FWHM is the full width at half its maximum intensity and θ is the half diffraction angle at which the peak is located.

Dislocation density δ ((lines/m<sup>2</sup>) value is related to the number of defects in the crystal. The value calculated from the average values of the crystallite size (D) by the following equation:

$$\delta = \frac{1}{D^2}$$

The strain  $\epsilon$  values were determined by using the following formula:

$$\epsilon = \frac{\beta_{hkl} \cos\theta}{4}$$

The calculated data such as  $V$ ,  $D$ ,  $\delta$  and  $\epsilon$  summarized in table 1 indicate that there is no difference among the values for the samples. The observation reveals that the crystallographic parameters are not changed by changing the reaction conditions. However, it is clear that reaction condition plays an important role on the purity and crystal phase growth of the samples. According to the data, increasing the reaction temperature increases the crystal growth of  $S_2$ . When the reaction time is increased to 96 h at 180 °C, the crystal growth is increases more ( $S_3$ ). But, when the reaction temperature is increased more to 200 °C, the crystal growth is decreased. The purity data reveal that increasing the reaction time and temperature has a negative effect on the purity of the obtained nanomaterials. The data reveals that the best condition for the synthesis of  $Sr_2Nb_2O_7$  nanomaterial in the present synthesis rout is 120 °C for 48 h.

### 3.2. Morphology Analysis

Figure 2 presents the FESEM images of the as prepared nanomaterials. The data indicate that the reaction time and temperature affect considerably on the morphology of the obtained targets. It is found that the morphology of  $S_1$  and  $S_3$  are flower. However, when the reaction time is increased, the morphology of the target is changed to a uniform nano plate structure for  $S_2$ . When the reaction time and temperature is increased more for  $S_3$  and  $S_4$ , the morphology is changed to flower and rod, respectively.

### 3.3. Optical Property

UV-Vis absorption spectra of the as-synthesized samples are shown in figure 4a. The direct optical band gap energy is also shown in figure 4b. The absorption data indicate that the as-synthesized nanocomposite possesses a typical visible absorption edge at about 400-420 nm. In general, the relation between the absorption coefficient and incident photon energy can be written as  $(\alpha h\nu)^2 = A(h\nu - E_g)$  for direct band gap energy. In this equation,  $A$  and  $E_g$  are constant value and direct band gap energy, respectively [31]. To measure the direct band gap energy, the linear part of the curve to the energy axis was extrapolated. It was found that the smallest direct band gap energy was about 3.05 to 3.10 eV.

### 3.4. Magnetic property

The magnetic property of  $S_1$  was investigated by VSM analysis. The magnetic hysteresis (M-H) curve of the sample is shown in figure 5 which provides the evidence that the nanomaterial shows ferromagnetic behavior at room temperature. The values of saturation magnetization ( $M_s$ ) is 0.02 emu/g for  $S_1$ .

### 3.5. Photocatalytic Study

Researchers utilize two different approaches to obtain the optimal conditions in chemical reactions, namely one-at-a-time and experimental design methods. Recently, the experimental design method receives more attention, since, different experiment factors affect each other and this is not considered in the one-at-a time approach. One of the basic designs is full factorial [32]. In this design, all possible combinations of the factors and their settings are simultaneously considered. Assume that there is  $k$  investigating variables and each variable could be set to  $m$  distinctive levels. So, the number of possible combinations of the factors and their settings is  $m^k$ . In chemical systems, three levels of the factor setting is common because such designs allow the determination of all main effects and all interaction effects with small number of experiment.

In full factorial method, the relation between factors and response is theoretically modeled which causes the reproducibility in the phenomenon under study to be able to experiment with it and to elucidate the results. Response surface methodology (RSM) is a mathematical and statistical method, which analyzes experimental design by applying an empirical model [33]. The adequacy of the applied model is checked using analysis of variance (ANOVA) which needs some replicate experiments [33].

In our study, in the MG pollutant dye degradation, the goal was to determine how much nanocatalyst should be used, and at which time and H<sub>2</sub>O<sub>2</sub> volume the degradation should be monitored. The response was the obtained degradation (%). Different possible combinations of these factors were designed which are reported in table 2. All the experiments were done at two days with random order. The central composite design (CCD) was chosen for modelling and optimization of the proposed procedure based on S<sub>1</sub>. A three-level CCD with three factors (H<sub>2</sub>O<sub>2</sub> (A) catalyst (B) and time (C)) was used to investigate the effects of factors. The condition of 20 experiments designed by CCD accompanied to dye degradation percentage (response (Y%)) are also given in table 2. The experimental range and levels of independent variables are shown in table 3. As shown in table 3, the independent variables (H<sub>2</sub>O<sub>2</sub> volume (A<sub>1</sub>), catalyst amount (A<sub>2</sub>) and stirring time (A<sub>3</sub>)) are given in the coded form (-α, -1, 0, +1, +α).

A typical experimental design photocatalytic reaction associated with the 2D and 3D plots and the residual plots to confirm the reliability of the calculated model to achieve the optimal conditions in the MG degradation process is included in the supplementary file.

The observed data of the factorial design was fitted to a quadratic response model. Prior to the analysis, low and high factor levels were coded to -1 and +1, respectively. Equation 1 shows the relation between the factors and the yield of the reaction, Y%, based on the first order model:

$$Y = +56.78 + 13.29 \times A + 9.22 \times B + 11.00 \times C + 1.00 \times A \times B - 5.75 \times A \times C + 2.25 \times B \times C - 4.89 \times A^2 + 0.41 \times B^2 - 0.47 \times C^2$$

(Equation 1)

Evaluation of the model quality was statistically performed by the analysis of variance (ANOVA) and the standard least squares techniques (Table 4). These analyses compare the differences between group means with the variability within the groups around the corresponding mean values. This ratio is called an F-distribution (F-value), varying from 1 to larger values. Values far from 1, exceeding from the tabulated F-value, provide evidence against the null hypothesis, indicating the significance of the regression parts of the fitted models. Equivalently, the null hypothesis is rejected when p-value is less than a significant level. In order to obtain the significant and reliable model at the 95% confidence level, the p-values for the fitted model and its corresponding terms should be smaller than 0.05. The p-value of the present regression was smaller than 0.05, showing that the model was significant at a high confidence level (95%) [33]. A further assessment of the fitted model can be carried out using the lack-of-fit test. Via this statistical test, the residual part is sub-divided into pure error and lack-of-fit. In other words, it distinguishes the random error from the systematic one, causing the lack of fit of the model with specific order. Therefore, at the 95% confidence level, the p-values for the lack-of-fits should be greater than 0.05, which is not significant. As shown in table 4, the outcomes of ANOVA are completely in agreement with the above statements.

Also the coefficient of determination (the R-square, adjusted-R-square) was used to express the quality of fit of polynomial model equation. In this case, R<sup>2</sup> of variation fitting for Y% indicated a high degree of correlation between the response and the independent factors (R<sup>2</sup> = 0.98). Also, the high value of adjusted regression coefficient (R<sup>2</sup>-adj = 0.96) indicated high significance of the proposed model. This means that, the difference between experimental and the predicted responses is negligible. Also the predicted R-squared value (0.87) was reasonable. The high accuracy and reliability of the developed mode for the determination of response value is shown in figure S<sub>1</sub>.

Figure 6 shows the dye degradation graphs for the obtained materials at the optimum conditions. Figure 6 a shows the dye volume effect on the degradation yield. It was found that at the ranges of 70 to 90 mL dye volume, the degradation was high; when the volume was increased more, the degradation was decreased considerably. It can be due to the decreasing the adsorption of dye on the catalyst making the process slower. Figure 6 b shows the reusability of S<sub>1</sub>. It indicates that the synthesized catalyst shows considerable reusability performance for the process until run 3. Figure 6 c shows the effect of dye concentration on the degradation yield. It is clear that the dye degradation percent was high when the dye concentration was in the ranges of 50 to 70 ppm. However, when the dye concentration was increased more up to 90 ppm, the degradation was decreased considerably. It seems that when the dye concentration is high, light wavelength cannot be penetrated into the dye solution (light screening effect) and/or reduced availability of active catalyst sites for MG molecules for adsorption and reaction. Figure 6 d presents the efficiency of MG degradation versus irradiation time. It is clear that the efficiency is low when the reaction time is spent until 20 min. However, when the irradiation time is increased more up to 80 min, the efficiency is increased considerably and reached to 95%.

Also, we studied the degradation of blank dye solution (without catalyst and H<sub>2</sub>O<sub>2</sub>) under the visible light irradiation at 60 min. It was found that the dye degradation was negligible for all of the conditions studied in figure 6. Besides, we investigated the degradation process at the optimized condition at the dark room. In the condition, the degradation yield was nearly zero.

## 4. Conclusion

This study describes the solvothermal synthesis of highly crystalline  $\text{Sr}_2\text{Nb}_2\text{O}_7$  nanomaterials. The XRPD patterns indicated that the  $\text{Sr}_2\text{Nb}_2\text{O}_7$  was crystallized well under solvothermal conditions. The magnetic hysteresis (M-H) curve of the  $\text{Sr}_2\text{Nb}_2\text{O}_7$  confirmed that the synthesized nanomaterial showed a ferromagnetic behavior at room temperature. It was found that the obtained materials had excellent efficiency for the removal of MG pollutant dye from aqueous solution. It was found that the optimum condition was 0.61 mL  $\text{H}_2\text{O}_2$ , 40 mg catalyst, 60 min. The degradation yield at the optimized conditions was 81% for  $\text{S}_1$ . Several tests were performed to investigate other parameters on the degradation yield. It was found that the catalyst performance at the concentration up to 70 ppm, and the dye solution volume up to 90 mL was excellent. Besides, the blank dye solution photodegradation was studied at the optimized reaction time. It was found that the degradation yield was negligible. Also, the degradation yield was investigated in the dark room at the optimized conditions. Langmuir–Hinshelwood (L–H) kinetic model data revealed that the heterogeneous photocatalytic process followed a first order reaction model.

## Reference

- [1] Fujimori Y, Izumi N, Nakamura T, *et al.* Application of  $\text{Sr}_2\text{Nb}_2\text{O}_7$  family ferroelectric films for ferroelectric memory field effect transistor. *Jpn J Appl Phys* 1998, **37**: 5207-5210.
- [2] Ishitani A, Kimura M. Unique method of patterning superconducting thin films by selective growth of Y–Ba–Cu–O. *Appl Phys Lett* 1990, **29**: 1076-1079.
- [3] Nanamatsu S, Kimura M, Kawamura T. Crystallographic and dielectric properties of ferroelectric  $\text{A}_2\text{B}_2\text{O}_7$  (A = Sr, B = Ta, Nb) crystals and their solid solutions. *J Phys Soc Jpn* 1975, **38**: 817-824.
- [4] Akishige Y, Kamata M, Fukano K. Successive phase transition of  $(\text{Sr}_{1-x}\text{Ba}_x)_2\text{Nb}_2\text{O}_7$ . *J Korean Phys Soc* 2003, **42**: 1187-1191.
- [5] Kato H, Kudo A. Photocatalytic decomposition of pure water into  $\text{H}_2$  and  $\text{O}_2$  over  $\text{SrTa}_2\text{O}_6$  prepared by a flux method. *Chem Lett* 1999, **33**: 1207-1210.
- [6] Hwang DW, Kim HG, Kim J, *et al.* Photocatalytic water splitting over highly donor-doped (110) layered perovskites. *J Catal* 2000, **193**: 40-48.
- [7] Machida M, Yabunaka J, Kijima T, Synthesis and photocatalytic property of layered perovskite tantalates,  $\text{RbLnTa}_2\text{O}_7$  (Ln = La, Pr, Nd, and Sm). *Chem Mater* 2000, **12**: 812-817.
- [8] Kudo A, Kato H, Nakagawa S. Water splitting into  $\text{H}_2$  and  $\text{O}_2$  on new  $\text{Sr}_2\text{M}_2\text{O}_7$  (M = Nb and Ta) photocatalysts with layered perovskite structures: factors affecting the photocatalytic activity. *J Phys Chem B* 2000, **104**: 571-575.
- [9] Domen K, Kondo JN, Hara M, *et al.* Photo- and mechano-catalytic overall water splitting reactions to form hydrogen and oxygen on heterogeneous catalysts. *Bull Chem Soc Jpn* 2000, **73**: 1307-1331.
- [10] Hwang DW, Lee LS, Li W, *et al.* Electronic band structure and photocatalytic activity of  $\text{Ln}_2\text{Ti}_2\text{O}_7$  (Ln = La, Pr, Nd). *J Phys Chem B* 2003, **107**: 4963-4977.
- [11] Mizoguchi H, Ueda K, Orita M, *et al.* Decomposition of water by a  $\text{CaTiO}_3$  photocatalyst under UV light irradiation. *Mater Res B* 2002, **37**: 2401–2406.
- [12] Chen D, Ye J. Selective synthesis of high performance single crystalline  $\text{Sr}_2\text{Nb}_2\text{O}_7$  nanoribbon and  $\text{SrNb}_2\text{O}_6$  nanorod photocatalysts. *Chem Mater* 2009, **21**: 2327-2333.
- [13] Brahmaraout B, Messing GL, McKinstry ST. Molten salt synthesis of anisotropic  $\text{Sr}_2\text{Nb}_2\text{O}_7$  particles. *J Am Ceram Soc* 1999, **82**: 1555-1565.
- [14] Prasadarao AV, Selvaraj U, Komarneni S. Sol–gel synthesis of strontium pyroniobate and calcium pyroniobate. *J Am Ceram Soc* 1992, **75**: 2697-2701.

- [15] Seraji S, Wu Y, Jewell-Larson NE. Patterned microstructure of sol-gel derived complex oxides using soft lithography. *Adv Mater* 2000, **12**: 1421-1424.
- [16] Jeong ED, Ha MG, Won MS, *et al.* Photophysical properties and electronic structure of highly donor doped (110) layered perovskite material. *J Korean Phys Soc* 2006, **49**: 671-674.
- [17] Lin B, Ma J, Yao Y, *et al.* Morphology controlled synthesis and characterization of  $\text{Sr}_2\text{Nb}_2\text{O}_7$  nanocrystalline powders by a solvothermal process. *J Am Ceram Soc* 2008, **91**: 1329-1331.
- [18] Ishizawa N, Marumo F, Kawamura T, *et al.* The crystal structure of  $\text{Sr}_2\text{Nb}_2\text{O}_7$ , a compound with perovskite-type slabs. *Acta Crystallogr Sect B* 1975, **31**: 1907-1912.
- [19] Schmalte HW, Williams T, Reller A, *et al.* A novel semiconducting perovskite-related phase:  $\text{Sr}_5\text{Nb}_5\text{O}_{17}$ . *Acta Crystallogr Sect C* 1995, **51**: 1243-1246.
- [20] Abrahams SC, Schmalte HW, Williams T, *et al.* Centrosymmetric or noncentrosymmetric: case study, generalization and structural redetermination of  $\text{Sr}_5\text{Nb}_5\text{O}_{17}$ . *Acta Crystallogr B* 1998, **54**: 399-416.
- [21] Elcoro L, Perez-Mato JM, Withers RL. Intergrowth polytypoids as modulated structures: a superspace description of the  $\text{Sr}_n(\text{Nb}, \text{Ti})_n\text{O}_{3n+2}$  compound series. *Acta Crystallogr Sect B* 2001, **57**: 471-484.
- [22] Williams T, Lichtenberg F, Widmer D, *et al.* Layered perovskitic structures in pure and doped  $\text{LaTiO}_{3.5x}$  and  $\text{SrNbO}_{3.5x}$ . *J Solid State Chem* 1993, **103**: 375-386.
- [23] Lichtenberg F, Herrnberger A, Wiedenmann K, *et al.* Synthesis of perovskite-related layered  $\text{AnBnO}_{3n+2} = \text{ABO}_x$  type niobates and titanates and study of their structural, electric and magnetic properties. *Solid State Chem* 2001, **29**: 1-70.
- [24] Sparks TD, Fuierer PA, Clarke DR. Anisotropic thermal diffusivity and conductivity of la-doped strontium niobate  $\text{Sr}_2\text{Nb}_2\text{O}_7$ . *J Am Ceram Soc* 2010, **93**: 1136-1141.
- [25] Ohi K, Kojima S. Successive phase transitions and their soft modes in ferroelectric  $\text{Sr}_2\text{Nb}_2\text{O}_7$ . *Jpn J Appl Phys* 1985, **24**: 815-817.
- [26] Yamamoto N, Yagi K, Honjo G, *et al.* New phases of  $\text{Sr}_2\text{Ta}_2\text{O}_7$  and  $\text{Sr}_2\text{Nb}_2\text{O}_7$  found by electron microscopy and diffraction. *J Phys Soc Jpn* 1980, **48**: 185-191.
- [27] Yamamoto N. High-resolution electron microscopy of the incommensurate structure in  $\text{Sr}_2\text{Nb}_2\text{O}_7$ . *Acta Crystallogr Sect A* 1982, **38**: 780-789.
- [28] Harsini SM, Darmokoesoemo H. [Electrochemical Degradation of Malachite Green Dye using Carbon/TiO<sub>2</sub> Electrodes](#). *J Mater Environ Sci* 2016, **7**: 1454-1460.
- [29] Hu KH, Meng M. Degradation of Malachite Green on  $\text{MoS}_2/\text{TiO}_2$  Nanocomposite, *Asian J Chem* 2013, **25**: 5827-5829.
- [30] Khezami L, Taha KK, Ghiloufi I, *et al.* [Adsorption and photocatalytic degradation of malachite green by vanadium doped zinc oxide nanoparticles](#). *Water Sci Technol* 2016, **73**: 881-889.
- [31] Pascual J, Camassel J, Mathieu M. Fine structure in the intrinsic absorption edge of  $\text{TiO}_2$ . *Phys Rev B* 1978, **18**: 5606-5614.
- [32] *Comprehensive Chemometrics Chemical and Biochemical Data Analyses*, Vol. 1, 2009, chapter 12, page 354.
- [33] Box GEP, Draper NR. *Empirical model-building and response surfaces*. Wiley: New York, 1987.
- [34] Hosseinpour Z, Alemi A, Khandar AA, *et al.* A controlled solvothermal synthesis of CuS hierarchical structures and their natural-light-induced photocatalytic properties. *New J Chem* 2015, **39**: 5470-5476.
- [35] Maria Magdalane C, Kaviyarasu K, Judith Vijaya J, *et al.* Photocatalytic activity of binary metal oxide nanocomposites of  $\text{CeO}_2/\text{CdO}$  nanospheres: Investigation of optical and antimicrobial activity. *J Photochem Photobiol B Biol* 2016, **163**: 77-86.

- [36] Tolia JV, Chakraborty M, Murthy ZVP. Photocatalytic degradation of malachite green dye using doped and undoped ZnS nanoparticles. *Pol J Chem Technol* 2012, **14**: 16-21.
- [37] Deepa N, Meghna P, Kandasamy S. Experimental studies on decolonisation of malachite dye using continuous photocatalytic reactor. *Int Res J Environ Sci* 2014, **3**: 14-21.
- [38] Hameed BH, Lee TW. Degradation of malachite green in aqueous solution by Fenton process. *J Hazard Mater* 2009, **164**: 468-472.
- [39] Abilarasu A, Somanathan T, Saravanan A, *et al.* Enhanced photocatalytic degradation of malachite green on spinel ferrite (Nickel/Magnesium Ferrite) under direct sun light. *Int J Pharm Chem Biol Sci* 2016, **7**: 93-99.
- [40] Khademinia S, Behzad M, Kafi-Ahmadi L, *et al.* Solvothermally Synthesized Strontium Arsenate Nanomaterial through Response Surface Methodology. *Z Anorg Allg Chem* 2018, **644**: 221-227.

## Tables

**Table 1:** Cell parameters data, grain size, dislocation density, strain, quantitative phase analysis and rietveld analysis refinement data for Sr<sub>2</sub>Nb<sub>2</sub>O<sub>7</sub> nanocomposites.

Sample	2 $\theta$	a(Å)	b(Å)	c(Å)	V(Å <sup>3</sup> )	FWHM (rad)	D	$\delta$	$\epsilon$	purity	Counts	R <sub>Bragg</sub>	R <sub>F</sub>	$\chi^2$
S <sub>1</sub>	23.90	3.89	26.54	5.70	588	0.0056	25	0.0016	1.3	50	139	1.77	0.817	1.74
S <sub>2</sub>	23.88	3.89	26.54	5.70	588	0.0056	25	0.0016	1.3	47	165	1.9	0.9	2.12
S <sub>3</sub>	23.88	3.92	26.66	5.66	592	0.0056	25	0.0016	1.3	45	270	2.59	1.1	2.48
S <sub>4</sub>	23.86	3.92	26.63	5.63	588	0.0056	25	0.0016	1.3	41	250	3.35	1.43	2.29

**Table 2:** Three-level full factorial design in photodegradation process.

A: H <sub>2</sub> O <sub>2</sub>	B: Catalyst	C: Time	Yield
0.5	0.03	45	53
0.5	0.03	45	56
1.0	0.03	45	68
0.5	0.03	45	58
0.2	0.02	30	19
0.2	0.04	30	29
0.2	0.04	60	66
0.8	0.02	60	58
0.5	0.03	70	73
0.5	0.03	45	57
0.5	0.03	45	59
0.8	0.02	30	53
0.5	0.03	19	36
0.5	0.03	45	58
0	0.03	45	16
0.8	0.04	60	81
0.2	0.02	60	49
0.5	0.01	45	38
0.5	0.05	45	76
0.8	0.04	30	65

**Table 3:** The experimental range and levels of independent variables in CCD.

Factor	Name	Units	Low Actual	High Actual	Low Coded	High Coded
<b>A</b>	H <sub>2</sub> O <sub>2</sub>	Numeric	0.2	0.8	-1	1
<b>B</b>	Catalyst	Numeric	0.02	0.04	-1	1
<b>C</b>	Time	Numeric	30	60	-1	1

**Table 4:** Analysis of variance for suggested model.

Source	Sum of Squares	df	Mean Square	F Value	p-value Prob > F	
<b>Model</b>	5893.68	9	654.8533	54.06646	< 0.0001	significant
<b>A-H<sub>2</sub>O<sub>2</sub></b>	2410.897	1	2410.897	199.0502	< 0.0001	
<b>B-Catalyst</b>	1160.799	1	1160.799	95.83867	< 0.0001	
<b>C-Time</b>	1652.5	1	1652.5	136.4349	< 0.0001	
<b>AB</b>	8	1	8	0.660502	0.4353	
<b>AC</b>	264.5	1	264.5	21.83784	0.0009	
<b>BC</b>	40.5	1	40.5	3.34379	0.0974	
<b>A<sup>2</sup></b>	344.6708	1	344.6708	28.45695	0.0003	
<b>B<sup>2</sup></b>	2.456079	1	2.456079	0.202781	0.6621	
<b>C<sup>2</sup></b>	3.19776	1	3.19776	0.264016	0.6185	
<b>Residual</b>	121.1201	10	12.11201			
<b>Lack of Fit</b>	98.28673	5	19.65735	4.304528	0.0675	not significant
<b>Pure Error</b>	22.83333	5	4.566667			
<b>Cor Total</b>	6014.8	19				

## Figures

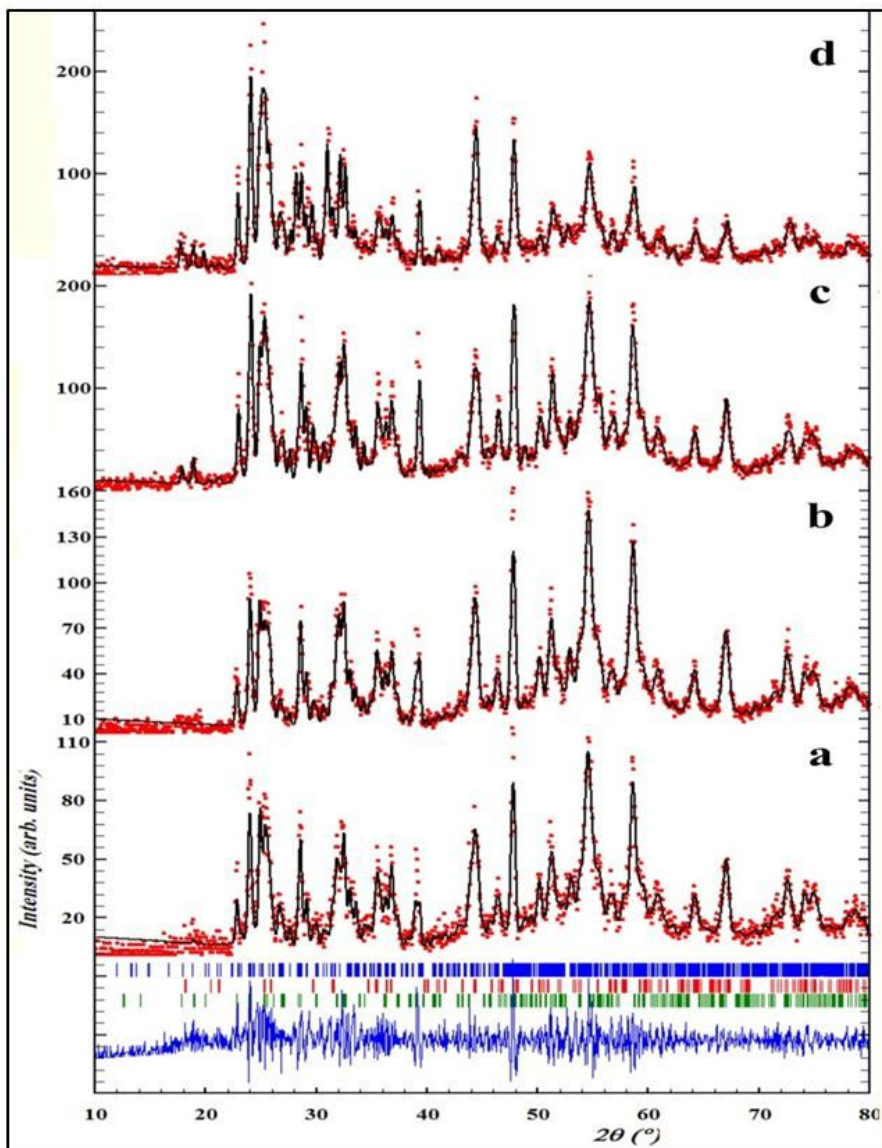
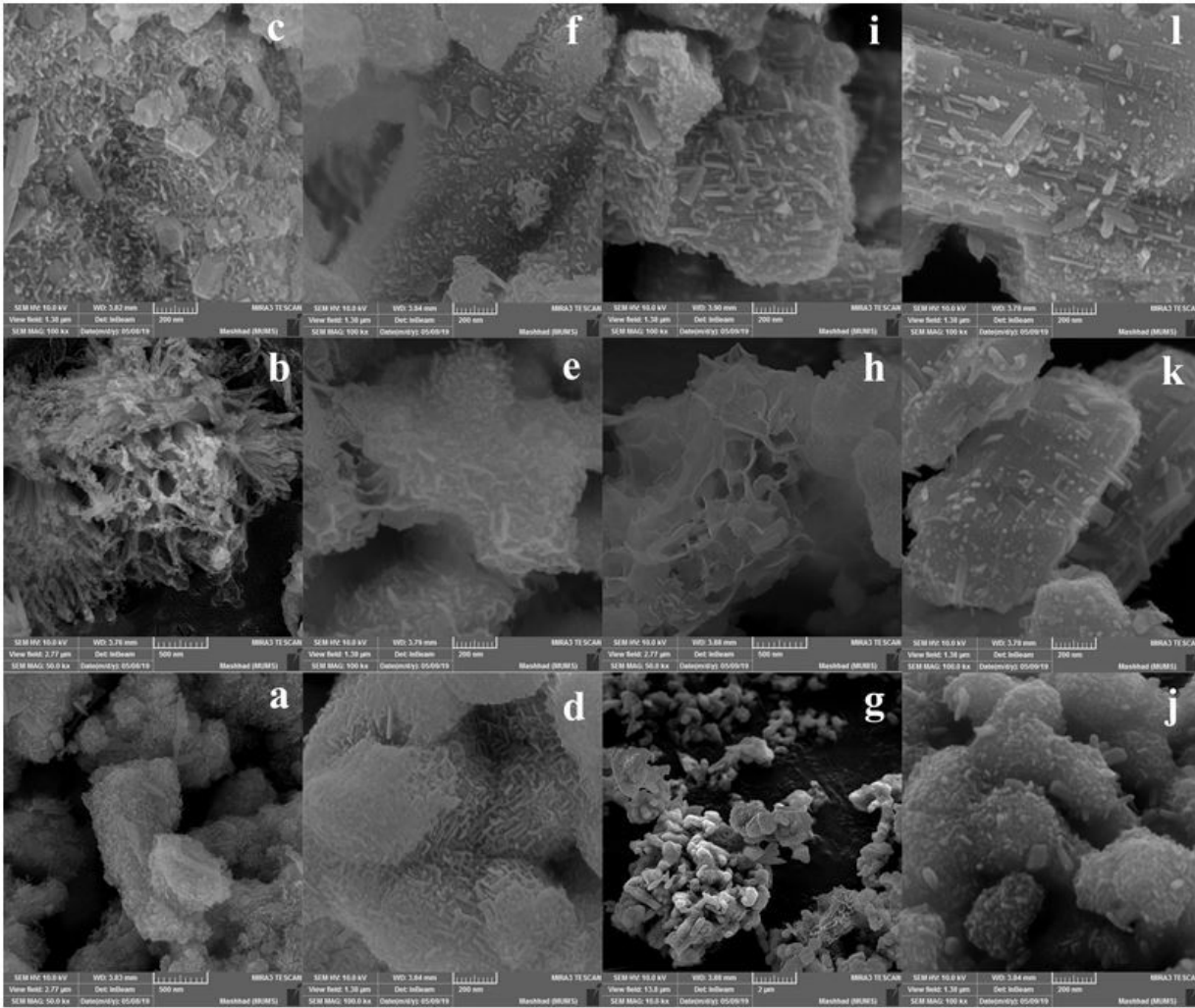


Figure 1

X-Ray powder diffraction patterns and the rietveld analyses of a) S1, b) S2, c) S3 and d) S4.



**Figure 2**

FESEM images of a-c) S1, d-e) S2, g-i) S3, j-l) S4.

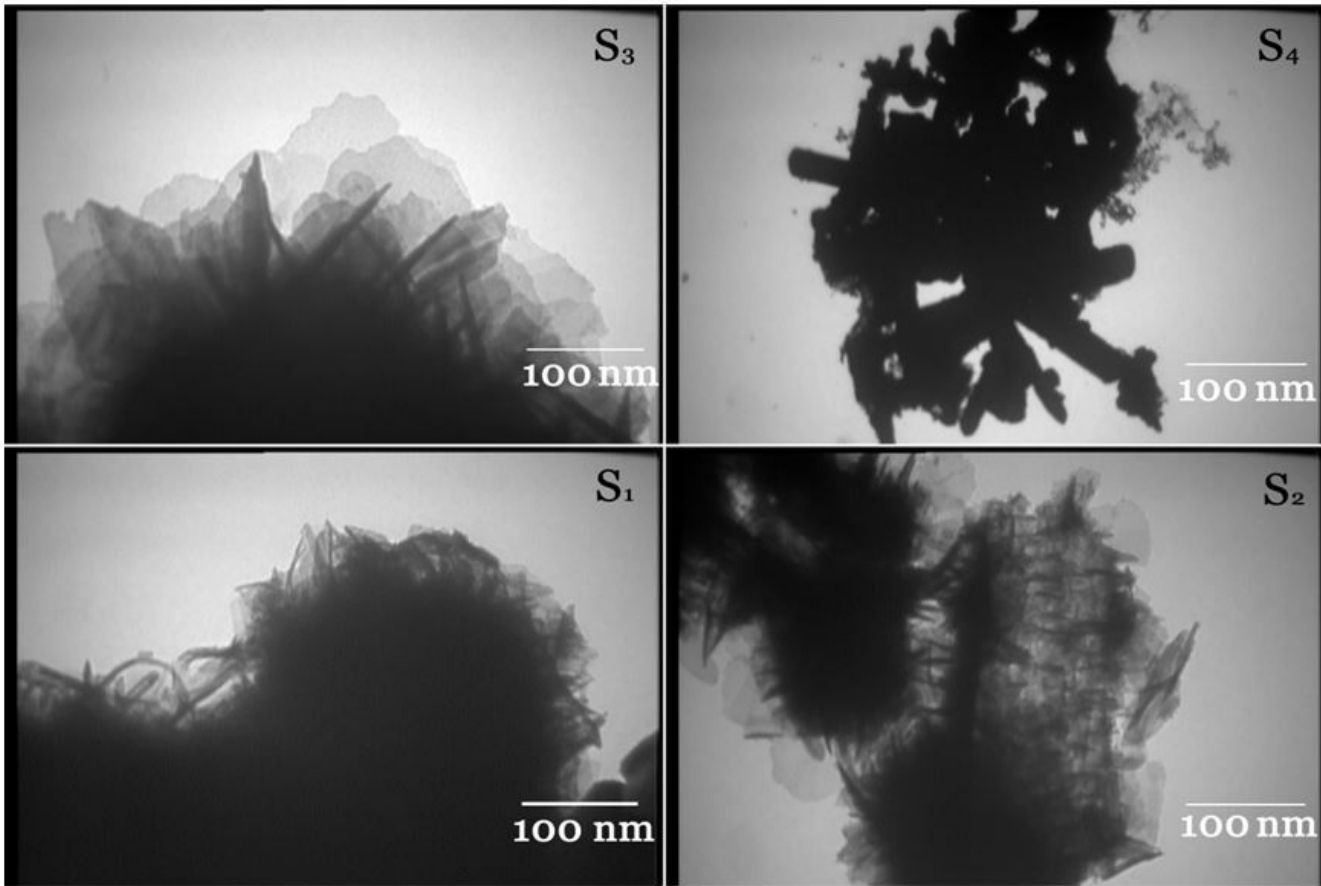


Figure 3

TEM images of the as-synthesized nanomaterials.

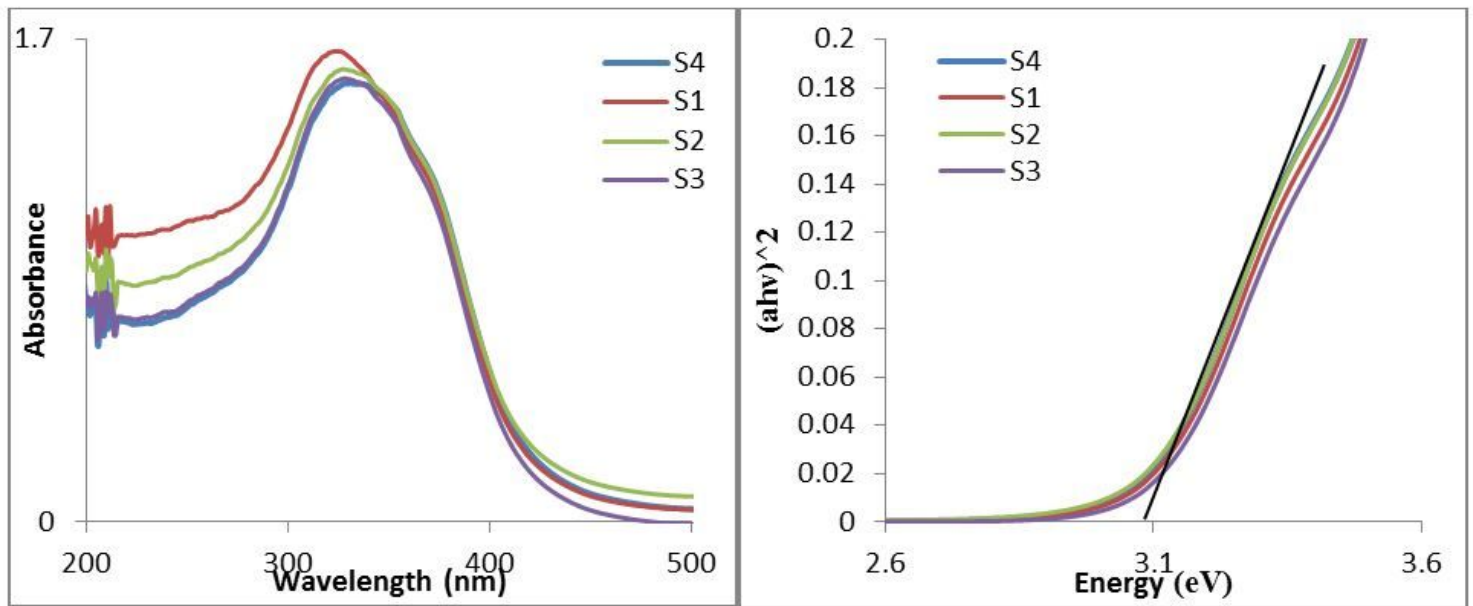
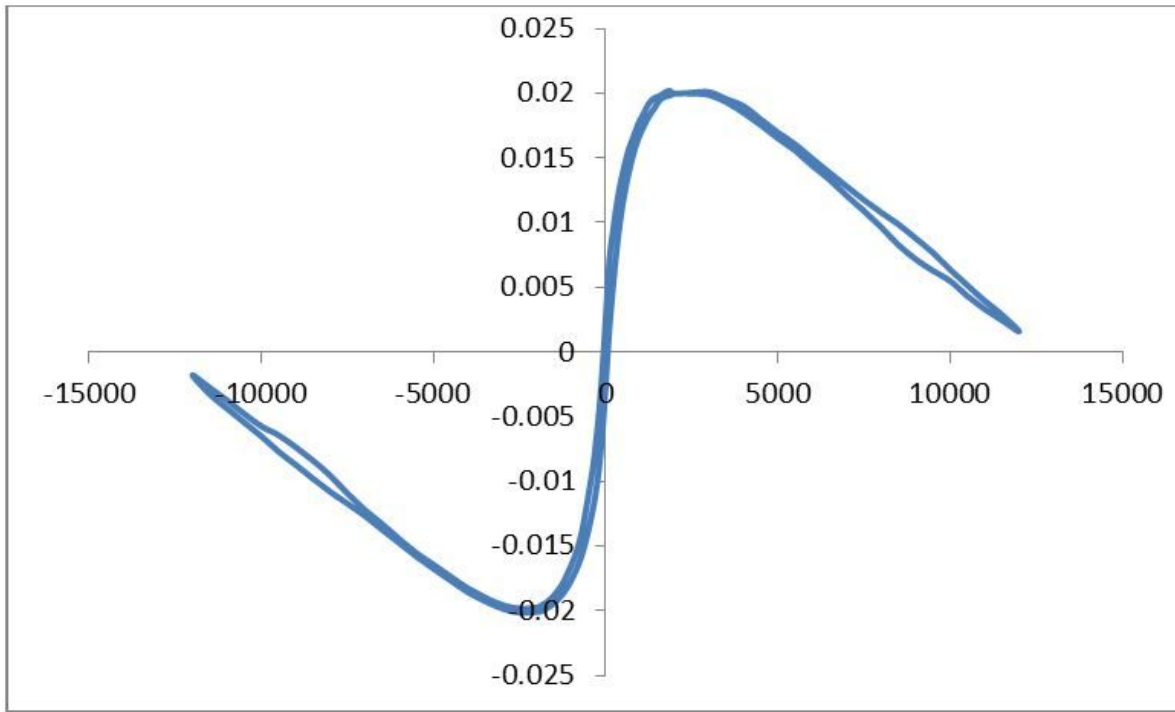


Figure 4

Plots of (a) UV-Vis spectra and (b)  $(\alpha h\nu)^2$  versus  $h\nu$  for the as-synthesized nanocomposites.



**Figure 5**

Room temperature M-H curves of S1.

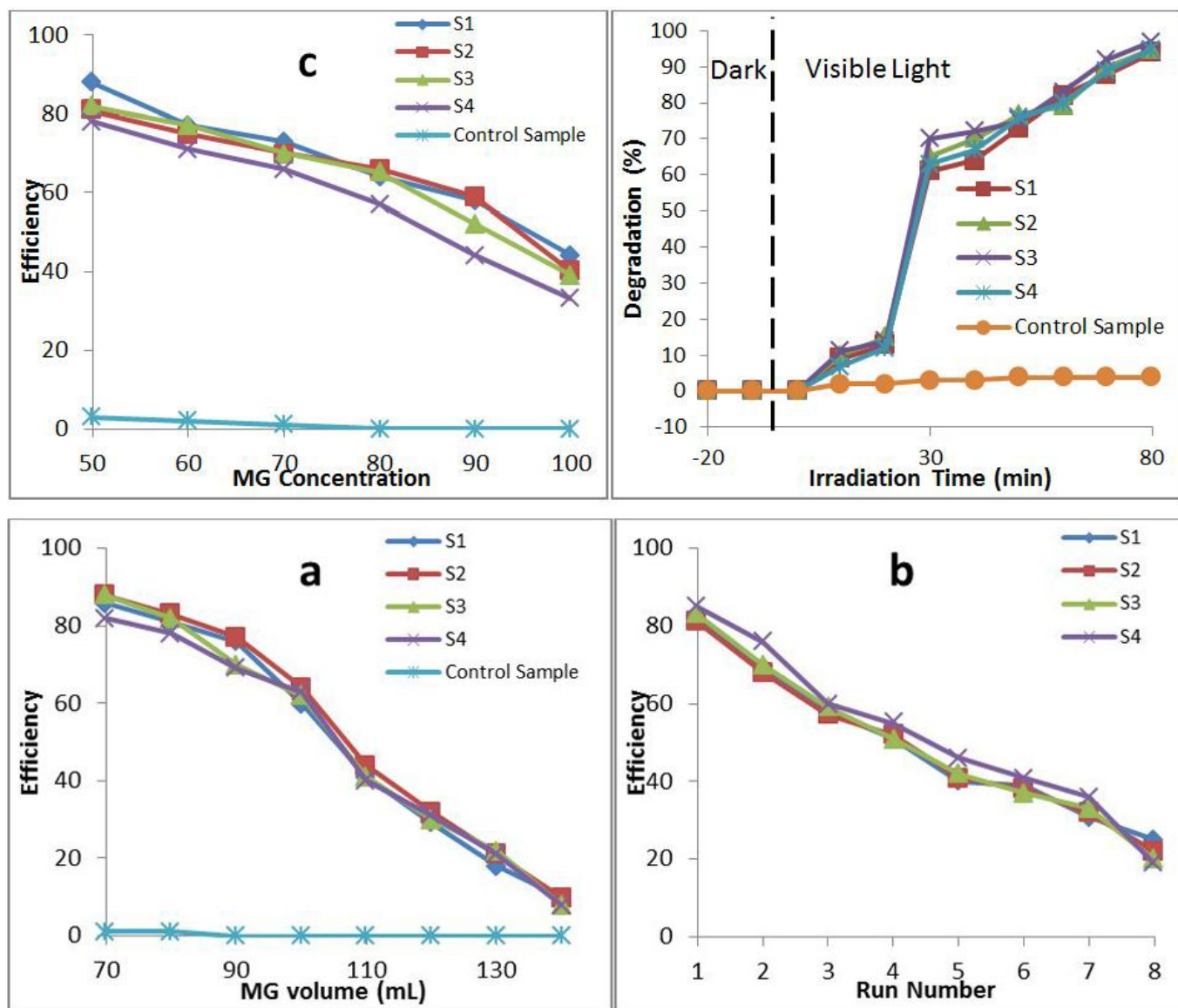


Figure 6

MG degradation (%) at (a) different MG volume, (b) reusability for S1, (c) different MG concentrations and (d) irradiation time.

## Supplementary Files

This is a list of supplementary files associated with this preprint. Click to download.

- [coverletter.docx](#)
- [coverletter.docx](#)
- [coverletter.docx](#)
- [supplementaryfile.docx](#)
- [supplementaryfile.docx](#)
- [supplementaryfile.docx](#)